



Improving Simulations of Warm Rain in a Bulk Microphysics Scheme

ROBERT CONRICK,^a CLIFFORD F. MASS,^a AND LYNN MCMURDIE^a

^a *Department of Atmospheric Sciences, University of Washington, Seattle, Washington*

(Manuscript received 10 February 2023, in final form 25 October 2023, accepted 31 October 2023)

ABSTRACT: Current bulk microphysical parameterization schemes underpredict precipitation intensities and drop size distributions (DSDs) during warm rain periods, particularly upwind of coastal terrain. To help address this deficiency, this study introduces a set of modifications, called RCON, to the liquid-phase (warm rain) parameterization currently used in the Thompson–Eidhammer microphysical parameterization scheme. RCON introduces several model modifications, motivated by evaluating simulations from a bin scheme, which together result in more accurate precipitation simulations during periods of warm rain. Among the most significant changes are 1) the use of a wider cloud water DSD of lognormal shape instead of the gamma DSD used by the Thompson–Eidhammer parameterization and 2) enhancement of the cloud-to-rain autoconversion parameterization. Evaluation of RCON is performed for two warm rain events and an extended period during the Olympic Mountains Experiment (OLYMPEX) field campaign of winter 2015/16. We show that RCON modifications produce more realistic precipitation distributions and rain DSDs than the default Thompson–Eidhammer configuration. For the multimonth OLYMPEX period, we show that rain rates, rainwater mixing ratios, and raindrop number concentrations were increased relative to the Thompson–Eidhammer microphysical parameterization, while concurrently decreasing raindrop diameters in liquid-phase clouds. These changes are consistent with an increase in simulated warm rain. Finally, real-time evaluation of the scheme from August 2021 to August 2022 demonstrated improved precipitation prediction over coastal areas of the Pacific Northwest.

SIGNIFICANCE STATEMENT: Although the accurate simulation of warm rain is critical to forecasting the hydrology of coastal areas and windward slopes, many warm rain parameterizations underpredict precipitation in these locations. This study introduces and evaluates modifications to the Thompson–Eidhammer microphysics parameterization scheme that significantly improve the accuracy of rainfall prediction in those regions.

KEYWORDS: Rainfall; Cloud microphysics; Cloud parameterizations; Model comparison; Model errors; Numerical weather prediction/forecasting

1. Introduction

Although microphysical parameterizations in numerical weather prediction (NWP) models have advanced over the past decades, there remains considerable uncertainty regarding liquid-phase (warm rain) microphysics and associated processes. Many recent studies investigating liquid-phase microphysics have focused on aerosol–cloud interactions (e.g., Lim and Hong 2010; Mansell et al. 2010; Thompson and Eidhammer 2014; Sena et al. 2016; Barros et al. 2018; Duan et al. 2019), while

others have developed more physically based representation of cloud-to-rain autoconversion and rain–cloud collection (e.g., Lee and Baik 2017; Ahmed et al. 2020; Zeng and Li 2020). Observations from the Olympic Mountains Experiment (OLYMPEX) during winter 2015/16 (Houze et al. 2017) indicate that warm rain contributes significantly to overall precipitation totals when landfalling midlatitude cyclones interact with the coastal terrain of the Pacific Northwest. Analysis of data collected during OLYMPEX suggested that warm rain periods in the region are characterized by high raindrop number concentrations and small raindrop diameters (Zagrodnik et al. 2018, 2019). Several studies have found underpredicted precipitation accumulation when warm rain is present (Colle et al. 1999; Colle and Mass 2000; Garvert et al. 2005a). More recent work by Minder et al. (2008) showed that precipitation was significantly underpredicted over the windward slopes of the Olympic Mountains of Washington State during heavy precipitation events (mainly atmospheric rivers).

Supplemental information related to this paper is available at the Journals Online website: <https://doi.org/10.1175/MWR-D-23-0035.s1>.

Corresponding author: Robert Conrick, robert.conrick@gmail.com

DOI: 10.1175/MWR-D-23-0035.1

© 2023 American Meteorological Society. This published article is licensed under the terms of the default AMS reuse license. For information regarding reuse of this content and general copyright information, consult the AMS Copyright Policy (www.ametsoc.org/PUBSReuseLicenses).

Other studies along the U.S. West Coast, including [Lin and Colle \(2009\)](#), [Lin et al. \(2013\)](#), [Darby et al. \(2019\)](#), [Conrick and Mass \(2019a,b\)](#), and [Naeger et al. \(2020\)](#) demonstrated that warm rain is underpredicted by mesoscale models using modern microphysical parameterizations even with increasing horizontal resolution. Underprediction of warm rain has also been noted in South Korea ([Min et al. 2015](#); [Song and Sohn 2018](#)) and along the west coast of South America ([Garreaud et al. 2016](#); [Massmann et al. 2017](#); [Schumacher et al. 2020](#)).

Recent simulations of weather systems over the Pacific Northwest ([Conrick and Mass \(2019a,b\)](#)) demonstrated that current microphysics schemes underpredict precipitation within the warm sector of midlatitude cyclones, where melting levels are high and moisture is abundant—conditions often coincident with warm rain development. [Conrick and Mass \(2019b\)](#) found that underpredicted precipitation was accompanied by simulated raindrop size distributions with larger and fewer raindrops than observed, implying that models struggled to produce the microphysical characteristics of warm rain. [Naeger et al. \(2020\)](#) analyzed similar precipitation events as [Conrick and Mass \(2019b\)](#) using the same model and noted similar deficiencies during warm rain periods.

Deficiencies in simulating warm rain have been noted regardless of which model or bulk parameterization is used. For example, the studies by [Colle et al. \(1999\)](#), [Colle and Mass \(2000\)](#), [Garvert et al. \(2005a\)](#), and [Minder et al. \(2008\)](#) used the fifth-generation Penn State–NCAR Mesoscale Model (MM5), whereas later studies applied the Weather Research and Forecasting/Advanced Research WRF (WRF-ARW) Model with various microphysics parameterizations. Recently, [Conrick and Mass \(2019b\)](#) and [Naeger et al. \(2020\)](#) examined precipitation and rain DSD characteristics from several WRF microphysics schemes, finding that warm rain biases occurred across models and microphysical parameterizations. Importantly, synoptic and mesoscale conditions varied considerably in these studies. Thus, specific moisture or airflow configurations are unlikely to cause the precipitation bias, suggesting there may be a common deficiency in currently available bulk microphysical parameterization schemes.

To address these liquid-phase microphysical deficiencies, this study presents and evaluates a series of modifications—called RCON—to the Thompson–Eidhammer microphysics scheme ([Thompson and Eidhammer 2014](#)). RCON is based on the introduction of a new autoconversion parameterization ([Nickerson et al. 1986](#)) and its requirement of a lognormal cloud water droplet size distribution, which is parameterized to be wider than the gamma distribution used by Thompson–Eidhammer. As a result, we incorporate two major model changes to the Thompson–Eidhammer microphysics scheme: 1) the use of a wider lognormal cloud water DSD and 2) enhancement of the cloud-to-rain autoconversion parameterization.

Using data from the OLYMPEX campaign, this study shows that these model modifications improve the representation of warm rain when compared to observations. The model modifications increase precipitation over coastal areas and windward slopes of the Pacific Northwest, regions where previous model evaluations have noted underprediction. The next section, [section 2](#), introduces and describes our model modifications, with subsequent sections providing an evaluation of its regional performance.

2. Description of the RCON microphysical modifications

In this section, we describe our microphysical parameterization modifications, hereafter known as RCON, which are a collection of changes to the liquid-phase (warm rain) portion of the Thompson–Eidhammer microphysical parameterization scheme (hereafter TE14) in the WRF-ARW Model ([Skamarock et al. 2008](#)). [Appendix A](#) provides a brief overview of the TE14 parameterization and [appendix B](#) outlines model configuration details.

The use of a lognormal cloud droplet size distribution (DSD) in RCON is a significant departure from the TE14 scheme, which employs a gamma distribution for its cloud DSDs. A lack of low-level cloud DSD observations from the OLYMPEX campaign precludes an observation-based analysis of cloud DSDs over the region. However, implementation of the lognormal cloud DSD was motivated by evaluating output from the Hebrew University of Jerusalem Israel (HUJI) bin microphysics (SBM) scheme ([Shpund et al. 2019](#)) during simulations of warm rain events over western Washington State. [Appendix A](#) provides more information about the SBM.

There is precedent for developing bulk microphysics schemes based on output from bin model simulations or parameterizations that are based on the stochastic collection equation. While not an exhaustive list, examples include the warm rain parameterization of [Khairoutdinov and Kogan \(2000\)](#), the parameterizations of [Seifert and Beheng \(2001, 2006\)](#), portions of the [Thompson et al. \(2008\)](#) and Thompson–Eidhammer schemes ([Thompson and Eidhammer 2014](#)), and bin-based parameterizations of autoconversion ([Lee and Baik 2017](#)) and collection ([Ahmed et al. 2020](#); [Zeng and Li 2020](#)).

The RCON modifications were developed using data from two warm rain events: 20 September 2015 and 15 February 2016. These events produced significant accumulations of warm rain over the Olympic Peninsula of Washington State over a prolonged period and were sampled by a sophisticated network of ground-based sensors, including disdrometers and vertically pointing radars. The meteorological and microphysical characteristics of these events are described in supplement 1 in the online supplemental material.

The SBM produced a more realistic distribution of simulated precipitation than TE14, as shown in [Fig. 1](#), suggesting that the SBM is producing a more accurate representation of liquid-phase microphysics, which includes cloud and rain DSDs. In both cases, the TE14 simulation produced substantially less precipitation than the SBM along coastal areas and windward slopes of the Olympic Mountains (the dashed analysis region of [Fig. 1](#); observing locations and terrain shown in [Fig. S1](#)). Significant underprediction by TE14, relative to observed precipitation, was present over the region. During the 20 September 2015 (15 February 2016) event, the use of the SBM scheme increased mean precipitation by 8.5 mm (10.9 mm) over the analysis region compared to the TE14 simulation, corresponding to a mean increase of approximately 41% (47%) in coastal/windward precipitation. Correlations (r) between simulated and observed precipitation improved when the SBM was used, increasing from $r = 0.85$ (TE14 vs Observed) to $r = 0.93$ (SBM vs Observed) during

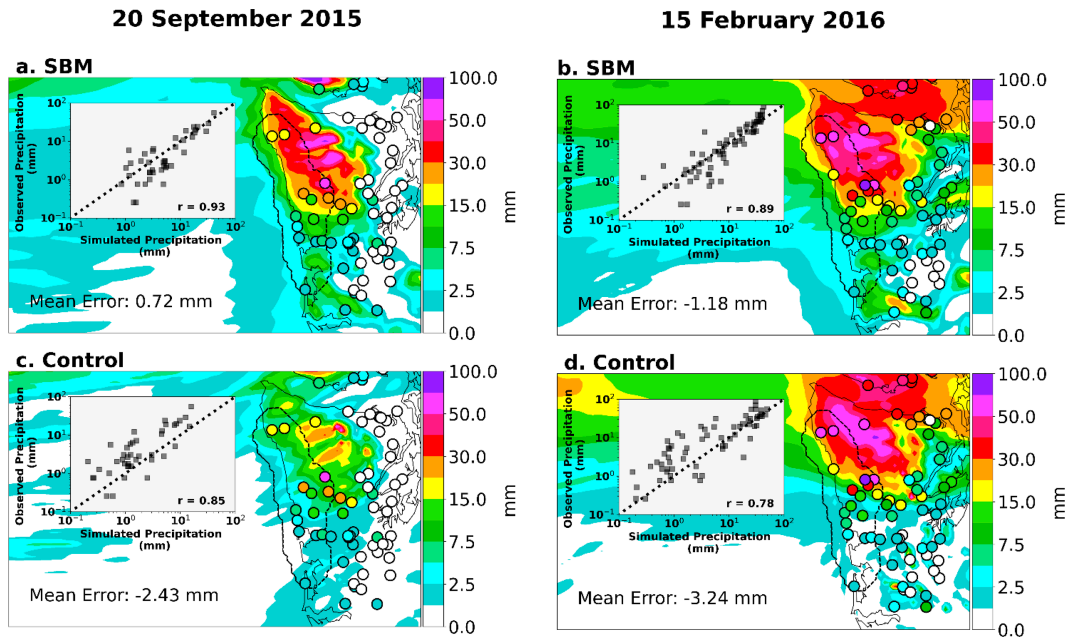


FIG. 1. Maps of precipitation (colored contours) from the WRF-ARW Model using (top) the SBM and (bottom) Control (TE14) simulations compared to observed precipitation (colored circles) for (left) the 20 Sep event and (right) the 15 Feb event. An inset scatterplot in each panel compares simulated and observed precipitation. The 1:1 line is shown in each inset panel. The coastal/windward region referenced in the text is outlined by a dashed contour.

the 20 September event, with a similar increase in correlation coefficient noted during the 15 February event (Fig. 1).

Observed and SBM-simulated mean rain DSDs at two OLYMPEX disdrometer¹ sites (Beach and Fishery; locations in Fig. S1) exhibited similar shapes and concentrations across diameter bins (Fig. 2). In contrast, TE14 produced rain DSDs with significantly fewer drops than observed, except at the largest diameters where TE14² produced too many large raindrops. Previous work by Conrick et al. (2019a,b) and Naeger et al. (2020) have noted that the rain DSDs produced by TE14 are more consistent with cold rain than warm rain.

With the above evaluation demonstrating that the SBM produced more realistic precipitation distributions and rain DSDs than TE14 during these events, the remainder of this section is used to outline the model modifications that distinguish RCON from the default configuration of TE14, which were motivated by SBM simulations.

a. Using a wider (lognormal) cloud DSD

The realistic prediction of cloud water DSDs is a necessary precursor to accurately predicting warm rain. From the SBM simulations presented above, we collected cloud water DSDs over coastal and windward regions of the Olympic Peninsula

(dashed region of Fig. 1) and compared them against the gamma distribution used by TE14 and against the lognormal distribution used by RCON (Fig. 3). The RCON model modifications utilize a nontruncated³ lognormal cloud DSD derived from the SBM DSDs instead of observed cloud DSDs, as none were available for these events. For the RCON distribution shown by Fig. 3, bulk DSD quantities (Q_C and N_C) were extracted from the SBM simulation and used to calculate the necessary distribution parameters (i.e., width and intercept). For reference, Table 1 presents the mathematical formulation of gamma and lognormal distributions as applied to cloud droplet distributions.

The narrow width of the TE14 gamma distribution is a key result from Fig. 3. To address this, we opt to use a significantly wider lognormal distribution in our RCON modifications. A wider gamma distribution will also increase precipitation rates, but not to the same degree of accuracy as RCON as described in this section. Specifically, the width parameter of the lognormal distribution (Table 1; σ) is optimized by using a method of moments applied to the SBM data. We hypothesize that the use of a wider cloud water distribution is more realistic, particularly during warm rain events where cloud droplets grow by collision-coalescence until they are large enough to precipitate out of the atmosphere.

Simulating the width of cloud DSDs presents a significant challenge due to a lack of observations of cloud water

¹ The PARSIVEL² disdrometers deployed during OLYMPEX are most accurate for hydrometeors within the 0.3–25 mm. At very small diameters below 0.3 mm, PARSIVEL disdrometers tend to undersample raindrops, resulting in the observed decrease in drop concentrations in those bins (Thurai et al. 2017, 2019).

² TE14 assumes an inverse exponential shape for its rain DSDs.

³ A “non-truncated” cloud DSD uses all drop diameters above 0 μm to calculate integral parameters such as mass or number mixing ratio. The majority of currently available WRF bulk microphysics parameterization schemes use non-truncated distributions.

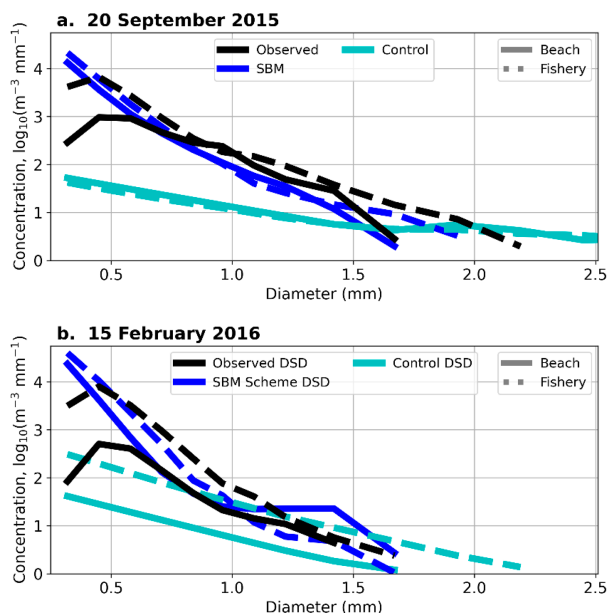


FIG. 2. Observed (black) and simulated (colors; see legend) mean rain DSDs during the warm rain periods of (a) 20 Sep 2015 and (b) 15 Feb 2016 at the Beach (solid) and Fishery (dashed) disdrometer sites. Only bins with concentrations of at least $1 \text{ m}^{-3} \text{ mm}^{-3}$ are included and only DSDs with $Q_R > 10^{-6} \text{ kg}^{-1} \text{ kg}^{-1}$.

distributions during warm rain precipitation in the region. Studies such as Wang et al. (2008) have shown that wider cloud DSDs have higher concentrations of large cloud droplets and are correlated with enhanced warm rain production. However, observed widths appear to be biased toward smaller values, possibly due to most observations being obtained in nonprecipitating clouds or in shallow stratocumulus (e.g., Miles et al. 2000; Geoffroy et al. 2014).

In TE14, the gamma DSD width parameter (μ) is a function of cloud droplet number concentration, as shown in Eq. (1):

$$\mu = \max\left(15, \frac{1 \times 10^9}{N_C} + 2\right). \quad (1)$$

This bounds μ between 2 and 15 based on the number of cloud droplets ($N_C; \text{m}^{-3}$).

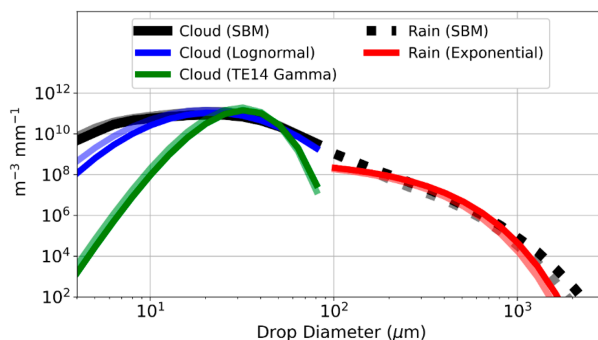


FIG. 3. Mean liquid water DSDs (cloud and rain) from simulations for the 20 Sep 2015 (transparent) and 15 Feb 2016 (opaque) events, with data obtained from the dashed area in Fig. 7. The discontinuity in the middle of the graph shows the dividing diameter ($80 \mu\text{m}$) between cloud and rain in the SBM scheme. Only bins with concentrations of at least $1 \text{ m}^{-3} \text{ mm}^{-3}$ are included where parent DSDs have $N_C > 10^3 \text{ kg}^{-1}$ and $Q_C > 10^{-6} \text{ kg}^{-1} \text{ kg}^{-1}$.

In contrast, the lognormal width parameter (σ) used by RCON is a function of the cloud water mass mixing ratio ($Q_C; \text{g m}^{-3}$) and the cloud droplet number concentration ($N_C; \text{m}^{-3}$), derived from SBM simulations of 20 September 2015 and 15 February 2016 [Eq. (2)]:

$$\sigma = \begin{cases} 0.2, & \text{if } \delta > 5.5 \times 10^{-4}, \\ (-1.19 \times 10^3)\delta + 0.815, & \text{if } 0.9 \times 10^{-4} > \delta > 5.5 \times 10^{-4}, \\ 0.7, & \text{if } \delta > 0.9 \times 10^{-4}, \end{cases} \quad (2)$$

where $\delta = (Q_C/N_C)^{1/3}$. Appendix C describes the process by which we produced the above expression for σ based on Q_C and N_C from the SBM simulations.

Because RCON uses a significantly wider cloud DSD than TE14, it follows to investigate whether optimizing μ to match RCON's σ will result in improved precipitation simulations. To do this, we related μ to σ using data obtained from the SBM simulations. An altered expression for μ was then used in the TE14 scheme (hereafter called the TE14_MU experiment; see supplement 2). Figure 4 shows simulated precipitation from the 20 September 2015 and 15 February 2016 warm rain events. The TE14_MU simulation did increase precipitation across coastal and windward regions of the Olympic

TABLE 1. Mathematical expressions for gamma and lognormal cloud water distributions, including a description of their terms with units.

	Equation	Description of terms
Gamma	$N(D) = N_0 D^\mu e^{-\lambda D}$	$N(D)$: No. of drops of diameter D (m^{-4}) N_0 : Intercept parameter (m^{-4}) λ : Slope parameter (m^{-1}) μ : Shape parameter (dimensionless)
Lognormal	$N(D) = \frac{N_T}{\sqrt{2\pi}D\sigma} \exp\left\{-\frac{1}{2}\left[\frac{\ln\left(\frac{D}{\widetilde{D}_N}\right)}{\sigma}\right]^2\right\}$	$N(D)$: No. of drops of diameter D (m^{-4}) N_T : Total drop concentration (m^{-3}) σ : Distribution width (dimensionless) \widetilde{D}_N : Median droplet diameter (m)

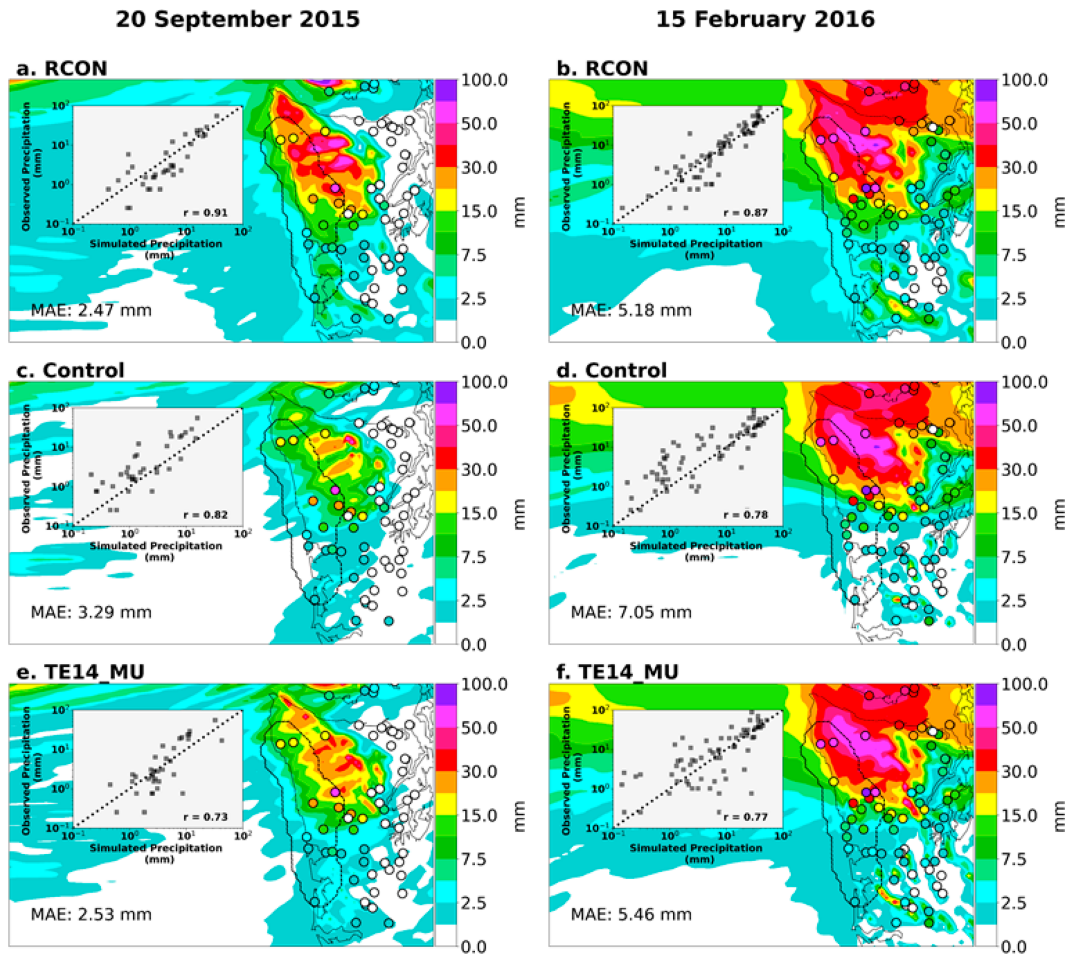


FIG. 4. Maps of simulated precipitation (colored contours) from (top) RCON, (middle) the Control, and (bottom) the TE14_MU experiment simulations compared to observed precipitation (colored circles) for the 20 Sep 2015 and 16 Feb 2016 warm rain events. Each map includes an inset scatterplot comparing simulated and observed precipitation at the stations shown on each map. The 1:1 line is shown in each inset panel.

Peninsula, but increases were generally less than 10 mm everywhere and were still less than produced by RCON.

Mean absolute errors (MAE) from TE14_MU improved by approximately 25% compared to TE14 (the Control), though correlations with observations were comparable between the two TE14 simulations. In contrast, RCON produced a more accurate simulation of precipitation characterized by lower MAE and higher correlations than either the Control or TE14_MU (Fig. 4). While the mean absolute error (MAE), decreased in the TE14_MU simulations as a result of increased precipitation (Fig. 4) and was comparable to values from RCON, the correlation between simulated and observed precipitation did not improve relative to the Control when TE14_MU was used. This was driven in part by an increase in precipitation variance from TE14_MU.

While the full details and more extensive microphysical analysis of the TE14_MU sensitivity study can be found in supplement 2, the TE14_MU experiment shows that replacing the relatively narrow gamma DSD in TE14 with a much wider distribution did not significantly increase precipitation during

warm rain event. Therefore, it appears that RCON’s more realistic precipitation simulation results from a combination of a wider cloud DSD and the use of a reformulated, more active autoconversion parameterization that accounts for the modified cloud DSD. The next section discusses the autoconversion parameterization used by RCON.

Relatedly, the adequate representation of aerosols and the nucleation process is important to ensure a realistic simulation of cloud DSDs. Because the SBM and TE14 schemes differ dramatically in their representation of atmospheric aerosols, a comprehensive evaluation of aerosols and nucleation processes is well outside of the scope of this project. However, a series of sensitivity experiments⁴ conducted for the 15 February event, in which we adjusted the SBM’s aerosol size distribution, yielded

⁴ For these sensitivity experiments, the two smallest modes of the tri-modal maritime aerosol distribution used by the SBM were modified independently by a multiplier of either 0.5 or 2 in order to decrease or increase the number of simulated aerosols, respectively.

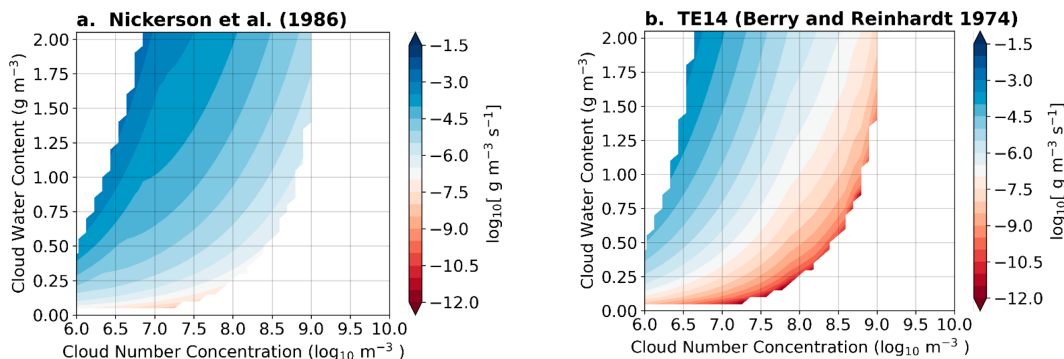


FIG. 5. The rain production rate due to autoconversion (dQ_R/dt ; $\text{g m}^{-3} \text{s}^{-1}$) from (a) RCON (Nickerson et al. 1986) and (b) TE14 (Berry and Reinhardt 1974) as a function of cloud water mass mixing ratio and cloud droplet number concentration.

cloud DSDs that were similar in shape to the SBM DSDs in Fig. 3, indicating a lack of sensitivity to specific environmental aerosol conditions (not shown). Additional information about aerosols in TE14 and SBM can be found in appendix B.

b. Autoconversion and other ancillary changes

RCON applies the Nickerson et al. (1986) parameterization for autoconversion, which is an adaptation of the Berry and Reinhardt (1974) autoconversion parameterization that requires use of a lognormal cloud DSD. The Berry and Reinhardt (1974) parameterization is presently used in TE14. Appendix D describes the modified autoconversion parameterization in greater detail, including how it was tuned to improve warm rain prediction. Compared to Berry and Reinhardt (1974), the Nickerson et al. (1986) parameterization increases autoconversion for all combinations of Q_C and N_C , resulting in a significant increase in the quantity of cloud water that is converted to rain (Fig. 5). As highlighted by Fig. 4 and as will be shown by our evaluations of RCON in the following section (section 3), the increased cloud-to-rain autoconversion rate plays a critical role in the ability of RCON to simulate warm-rain precipitation more accurately when it is coupled with a wider cloud water DSD (gamma or lognormal). Of course, it may be possible to adjust or tune parameters within the TE14 implementation of the Berry and Reinhardt (1974) parameterization to produce more warm rain,

though such a sensitivity experiment is generally outside the scope of this paper.

Other differences between TE14 and RCON include changes to calculations of cloud effective radii, droplet sizes, and number concentrations to be consistent with the revised cloud DSD (Table 2). The process rate calculations governing rain–cloud collection, cloud droplet evaporation, and the freezing of cloud droplets were also modified by replacing the pre-existing gamma cloud DSD with a lognormal distribution.

Finally, cloud water sedimentation is allowed to contribute to surface precipitation accumulations in RCON, similar to drizzle. Cloud water sedimentation results in only a slight increase in precipitation at the surface. For the 20 September 2015 and 15 February 2016 events, this change only slightly increased domain-averaged precipitation by 2.6% and 1.5%, respectively, mostly offshore of the Olympic Peninsula. The current TE14 scheme does not allow cloud water sedimentation to contribute to surface precipitation accumulations, though it can be easily modified to do so.

Regarding liquid precipitation, the RCON modifications retain the inverse exponential rain DSD from the TE14 scheme. This choice can be justified by observations that found precipitation-sized raindrops were generally well represented by an inverse exponential (e.g., Abel and Boutle 2012; Thurai et al. 2017, 2019). We recognize that other rain DSD shapes might improve warm rain prediction but defer the examination of such impacts to future work.

TABLE 2. Comparison of various microphysical properties of the gamma and lognormal cloud water distributions. Symbols not explained in the table are \bar{D}_N is the median droplet diameter, μ is the shape parameter of a gamma distribution, σ is the width parameter of a lognormal distribution, ρ_w is the density of water, λ is the slope of a gamma distribution, and $\Gamma(x)$ is the complete gamma function.

	Units	Gamma	Lognormal
Mean droplet diameter	m	$\frac{1 + \mu}{\lambda} = \left[\frac{\pi \rho_w N_T \Gamma(4 + \mu)}{6 Q_C \Gamma(1 + \mu)} \right]^{-1/3}$	$\bar{D}_N \exp\left(\frac{\sigma^2}{2}\right)$
Median volume diameter	m	$\frac{3.67 + \mu}{\lambda}$	$\bar{D}_N \exp(3\sigma^2)$
Cloud effective radius	m	$\frac{13 + \mu}{2 \lambda}$	$\frac{1}{2} \bar{D}_N \exp\left(\frac{5}{2}\sigma^2\right)$

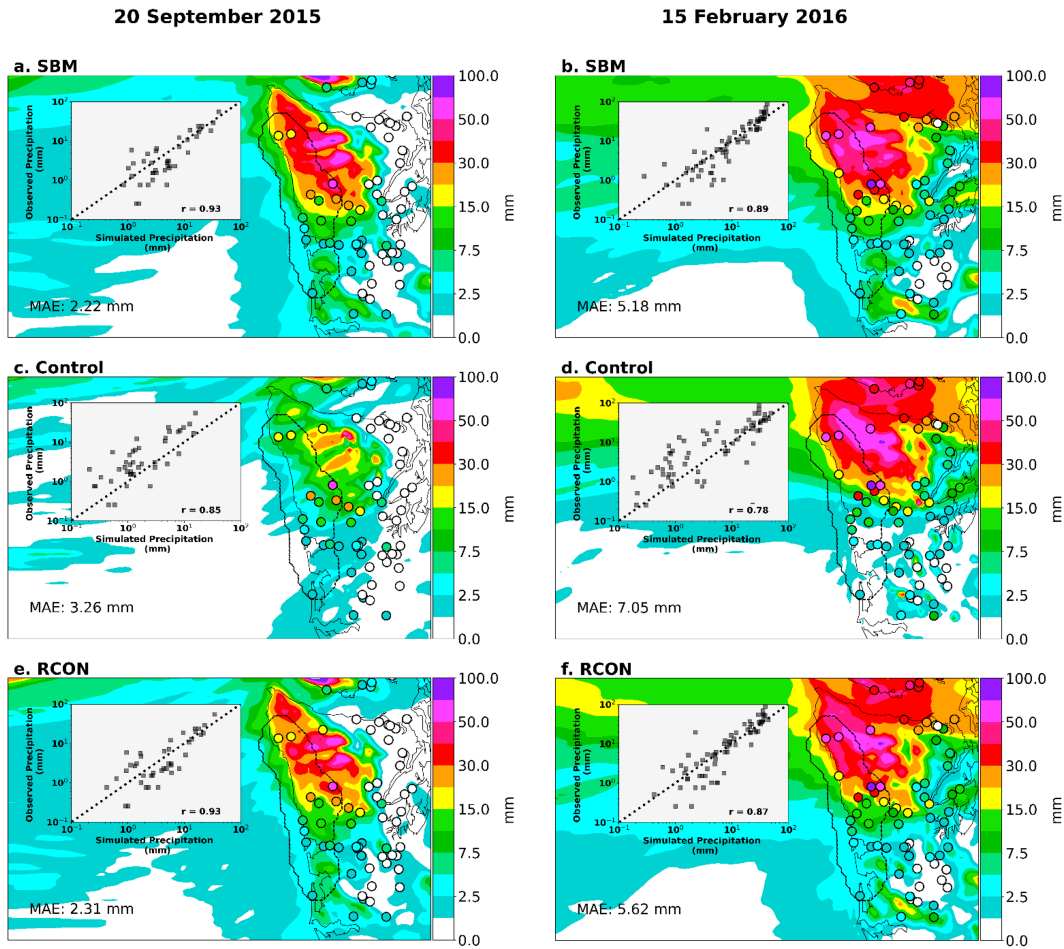


FIG. 6. Maps of simulated precipitation (colored contours) from (top) the SBM, (middle) the Control, and (bottom) the RCON simulations compared to observed precipitation (colored circles) for the 20 Sep 2015 and 16 Feb 2016 warm rain events. Each map includes an inset scatterplot comparing simulated and observed precipitation at the stations shown on each map. The 1:1 line is shown in each inset panel.

3. RCON performance evaluation

This section assesses the performance of RCON for a variety of meteorological conditions by first applying it to the 20 September 2015 and 15 February 2016 warm rain events. Subsequently, we simulate and evaluate an independent extended period (1 November–15 December 2015), and finally evaluate performance of RCON as a member of a real-time regional WRF ensemble forecasting system over a 1-yr period. In this section, simulations using TE14 microphysics are referred to as the Control simulation.

a. Performance during the 20 September 2015 and 15 February 2016 events

During both warm rain events, RCON produced precipitation accumulations over windward and coastal areas of the Olympic Peninsula that were larger in magnitude and more realistic than the Control (Fig. 6). For the 20 September 2015 event, mean simulated precipitation over the coastal/windward analysis region was 11.9 mm (RCON) and 4.5 mm (Control). For

the 15 February 2016 event, RCON mean precipitation was 14.4 mm compared to 13.0 mm from the Control over coastal/windward areas. The SBM and RCON simulations greatly increased precipitation accuracy over coastal areas. Indeed, the mean absolute precipitation error (MAE) from RCON during the 20 September 2015 event was 2.31 mm compared to 2.22 mm from the SBM and 3.26 mm from the Control. For the 15 February 2016 event, MAE from the RCON was 5.62 mm, the SBM MAE was 5.18, and the Control had a larger MAE of 7.05 mm. Correlations between observed and simulated precipitation also improved in RCON (0.87–0.93) compared to the Control (0.78–0.85). From these simulations, it appears that RCON is able to simulate precipitation that is qualitatively and quantitatively similar to the SBM, but at the computational cost of a bulk scheme.

Simulated rain DSDs at the Beach and Fishery sites, shown in Fig. 7, offer additional evidence that RCON is appropriately producing greater quantities of warm rain. Indeed, rain DSDs from the SBM, RCON, and observations exhibited quantitatively similar drop concentrations across diameter bins, with rain DSDs from RCON appearing more characteristic of warm

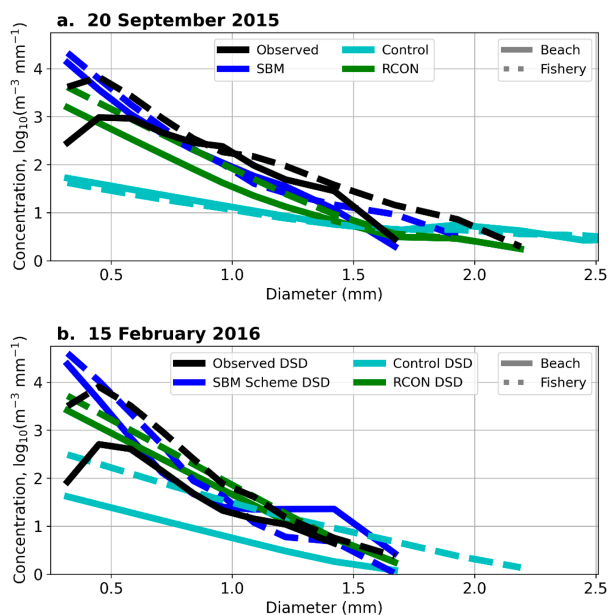


FIG. 7. Observed (black) and simulated (colors; see legend) mean rain DSDs during the warm rain periods of (a) 20 Sep 2015 and (b) 15 Feb 2016 from the Beach (solid) and Fishery (dashed) disdrometer sites. Only bins with concentrations of at least $1 \text{ m}^{-3} \text{ mm}^{-3}$ are included and only DSDs with $Q_R > 10^{-6} \text{ kg}^{-1} \text{ kg}^{-1}$.

rain than those simulated by the Control, i.e., there were substantially greater concentrations of small raindrops in RCON that were not simulated by the Control. Integrated quantities (i.e., number concentration, drop diameter, and liquid water content) from RCON also agreed well with observations, as did those from the SBM.

b. Extended period performance

Extended period simulations were performed using RCON and TE14 microphysics (the Control) for 1 November–15 December 2015, a subset of the anomalously wet OLYMPEX campaign. A 36- to 12-km domain configuration was used for this simulation, with results presented from the 12-km domain. Model configuration details can be found in appendix B, while supplement 3 documents the model's ability to realistically simulate synoptic conditions during this period.

To examine the impact of the RCON model modifications on warm rain over the extended period, we isolated periods of warm clouds by considering two parameters: 1) the height of the melting level and 2) the depth of cloud above the melting level. Warm rain processes are most likely when the melting level is higher in altitude (e.g., when temperatures in the lower troposphere are warm; Zagrodnik et al. 2018; McMurdie et al. 2018) and when the depth of cloud extending above the melting level is minimized (i.e., minimal or no ice present). At each of the ASOS/AWOS surface observing sites shown in Fig. 8, we determined the melting level height and the depth of cloud above the melting level from the extended-period simulation. To compute cloud depth, we applied a threshold of 90% to

relative humidity⁵ interpolated on 100-m height levels. Mean values of several microphysical variables in the lower atmosphere (0–2 km AGL) were examined as a function of the melting level height and cloud depth above the melting level. Clouds were considered warm if they extend less than 1 km above the melting level (AML). Observed precipitation is acquired for times when warm rain occurred in the Control simulation, as determined from the above method.

Observed warm rain accumulations during the extended period were compared against the RCON and Control simulations (Fig. 8). In general, RCON produced more precipitation than the Control and, therefore, significantly alleviated the rain underprediction that previous studies had noted during OLYMPEX. The largest benefit was noted along the Pacific coast, with more modest improvements around Puget Sound (western Washington) and in the Willamette Valley (western Oregon). The mean precipitation error from the Control and RCON simulations, calculated at all stations, was -14.1 and -4.2 mm, respectively, representing a significant improvement to regional precipitation prediction. Furthermore, if only stations within 50 km of the Pacific coast are considered, precipitation from RCON was nearly unbiased (0.6 mm) compared to -23.8 mm from the Control simulation. Non-warm rain periods experienced only minor changes, with mean errors of 57.9 mm from the Control simulation and 46.4 mm from RCON.

Consistent with the results from Fig. 8, simulated warm rain rates were heavier from RCON than the Control, with the largest differences coincident with melting levels greater than 2000 m AGL (Fig. 9a). Rain rate enhancement also occurred for mixed-phase clouds with high melting levels, where warm rain processes are also known to contribute to precipitation. Similarly, rainwater mixing ratio from RCON was larger than the Control in warm clouds with additional, but lesser, enhancement when cloud depths were 1000–2500 m above the melting level (Fig. 9b). Greater raindrop number concentrations were also simulated by RCON, resulting in smaller raindrop sizes compared to the Control (cf. Figs. 9c,d). This effect was particularly pronounced for clouds below the melting level, indicating that RCON produced precipitation that was more characteristic of warm rain compared to the Control. One might expect smaller raindrops to decrease precipitation rates since the sedimentation rate is a strong function of diameter. However, the larger concentration of small drops compensates for the smaller drops, therefore increasing warm rain rates.

Warm rain microphysical process rates involving cloud water are examined in Fig. 10. RCON increased rates of cloud-to-rain autoconversion (Fig. 10a) and rain–cloud collection (Fig. 10c). The greatest autoconversion enhancement occurred with moderate-to-high (>1500 m) melting levels and cloud extension less than 1000 m AML, both characteristic of warm rain environments. On the other hand, differences in rain–cloud collection were greatest in deeper, mixed-phase clouds (>1000 m AML; Fig. 10c), with lesser enhancement noted for liquid-phase clouds. Changes to

⁵ Relative humidity was chosen as a mostly independent measure of atmospheric moisture so that we were not using direct RCON output to evaluate the model.

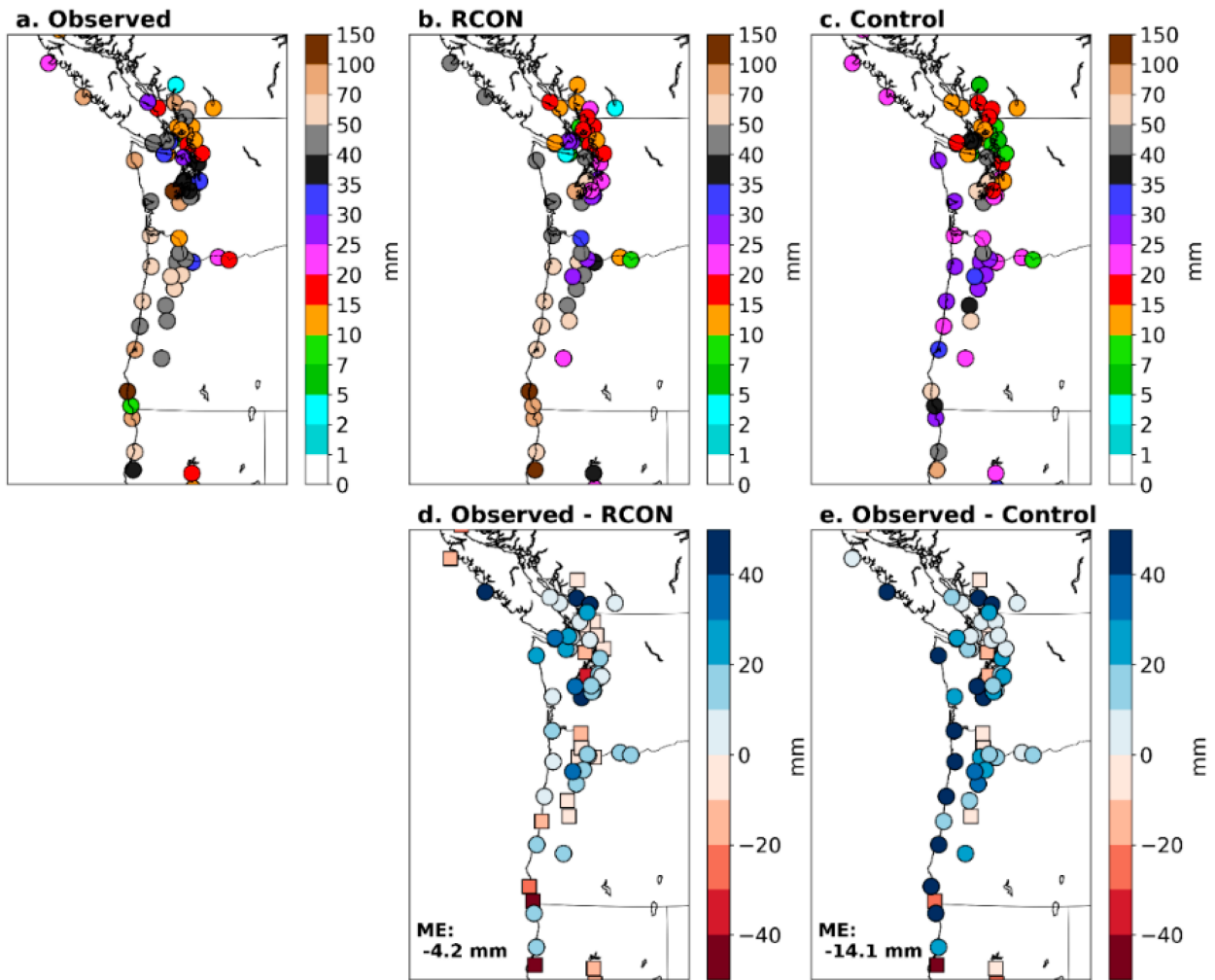


FIG. 8. Maps of simulated and observed warm rain accumulated during the extended period (1 Nov–15 Dec 2015). (a) Observations, (b) RCON, and (c) the Control. (d),(e) The difference between observed and simulated precipitation; red squares and blue circles denote over- and underprediction, respectively. Mean error (ME) is noted in (d) and (e).

process rates affecting cloud and raindrop number concentrations mirrored their mass mixing ratio counterparts, with more cloud droplets removed through autoconversion or coalesced into rain-sized particles than the Control (Figs. 10b,d).

c. Real-time RCON performance

RCON has been used operationally as a member of the University of Washington real-time WRF ensemble forecast system⁶ since mid-August 2021. The ensemble system comprises 24 members of varying physics and initial conditions. All ensemble members have 4-km grid spacing. Twenty-three of the 24 members use the Thompson et al. (2008) or Thompson–Eidhammer (Thompson and Eidhammer 2014) microphysics schemes, both of which use the same set of parameterized warm rain processes. The RCON member uses GFS initial and boundary

conditions. Appendix B provides more information about the WRF configuration.

In Fig. 11, we provide an evaluation of real-time 24-h accumulated precipitation forecasts over the Pacific Northwest from the 12-month period from August 2021 to August 2022. Mean precipitation error (forecast minus observed) from RCON is compared to that of the ensemble mean over five climatic and geographic regions of the Pacific Northwest (Washington and Oregon). While the use of RCON microphysics improved the accuracy of simulated precipitation across all regions, coastal areas experienced the greatest benefit. Indeed, the mean error along the Pacific Coast was reduced by approximately 75%—a significant improvement over the ensemble mean. In addition to more realistically simulated coastal precipitation, inland areas also experienced a reduction in mean error when RCON was used. Even over eastern Washington and Oregon, far away from the Pacific coast, RCON produced slightly more realistic quantities of simulated precipitation.

⁶ See <https://a.atmos.washington.edu/wrfrt/ensembles/> for additional information and to view daily RCON performance.

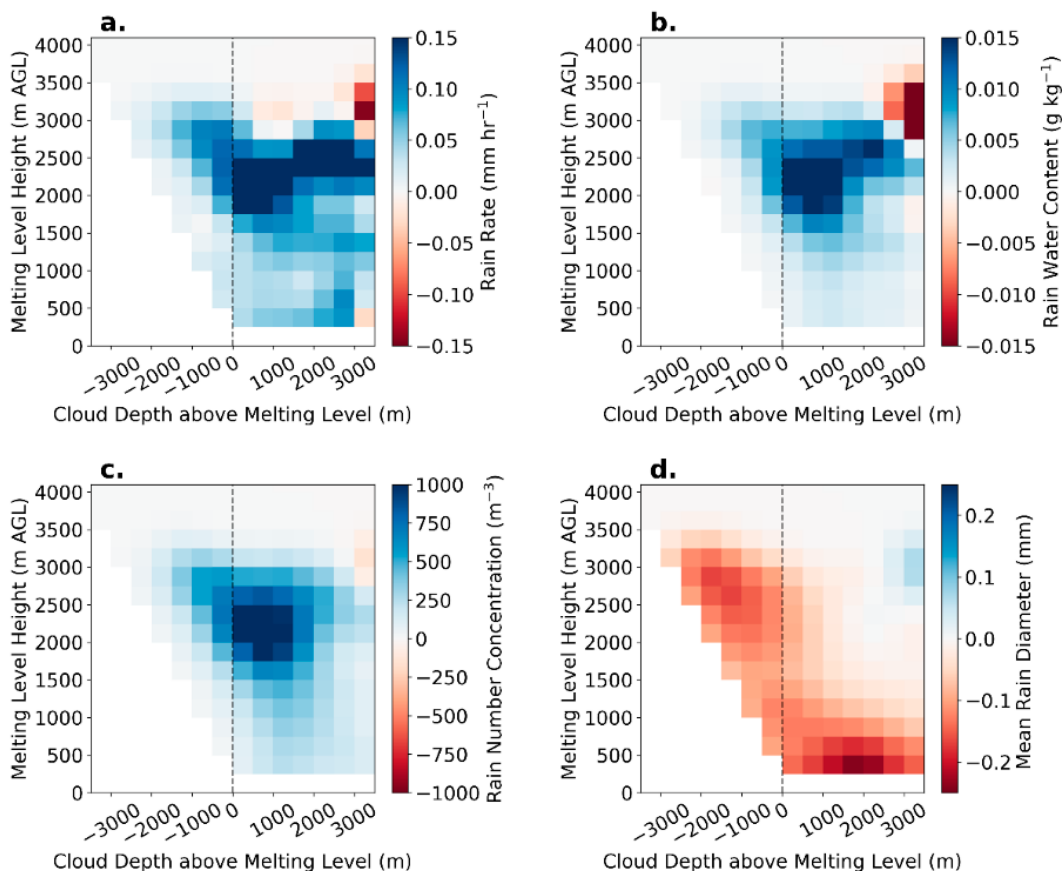


FIG. 9. Difference plots (RCON minus Control) for rain characteristics averaged over the 0–2 km AGL layer during the extended run for the locations shown in Fig. 8. The vertical axis depicts the melting-level height and the horizontal axis depicts the depth of cloud above the melting level. (a) The difference in rain rate, (b) the difference in rainwater mixing ratio, (c) the difference in rain number concentration, and (d) the difference in mean raindrop diameters. Data are only included when precipitation is present.

4. Discussion and conclusions

Contemporary bulk microphysical parameterization schemes generally underpredict precipitation over the coastal areas and windward slopes of the Pacific Northwest. This underprediction has been shown to occur in a variety of bulk microphysics schemes, with the errors most significant when warm rain is occurring or during periods favorable for warm rain development (e.g., Minder et al. 2008; Conrick and Mass 2019a,b; Naeger et al. 2020). Past model evaluation studies have shown that these simulated precipitation deficiencies are associated with errors in simulated number concentration, mass mixing ratio, and rain diameter during periods of warm rain (e.g., Conrick and Mass 2019b).

This study presents a series of modifications, called RCON, to the Thompson–Eidhammer (Thompson and Eidhammer 2014; TE14) aerosol-aware microphysics scheme. The RCON modifications introduce two major changes to TE14: 1) the use of a wider lognormal cloud water DSD, and 2) enhancement of the cloud-to-rain autoconversion parameterization. The introduction of these changes was motivated by analyzing the behavior of a bin microphysics scheme applied to warm rain events from the OLYMPEX campaign.

Evaluations of our microphysics modifications show great promise toward reducing simulated warm rain deficiencies. First, an evaluation was performed for the two warm rain events used to develop RCON: 20 September 2015 and 15 February 2016. Precipitation during both events was sampled by PARSIVEL disdrometers and rain gauges positioned around the Olympic Peninsula of Washington State. During both events, warm rain was observed for more than 12 h and was well simulated by the SBM and RCON simulations, both of which alleviated a substantial fraction of the coastal underprediction we documented. Rain DSDs simulated by RCON were more like those observed during warm rain events, with large concentrations of small drops.

Further model evaluation was conducted over an extended period during the OLYMPEX field campaign (1 November–15 December), encompassing a variety of synoptic-scale precipitation systems that impacted the Olympic Peninsula. By partitioning the period into warm and cold rain events based on melting level and the cloud depth above the melting level, it was demonstrated that rain rate, rainwater mixing ratio, and raindrop number concentration were increased in warm clouds when RCON modifications were used. The increased rain

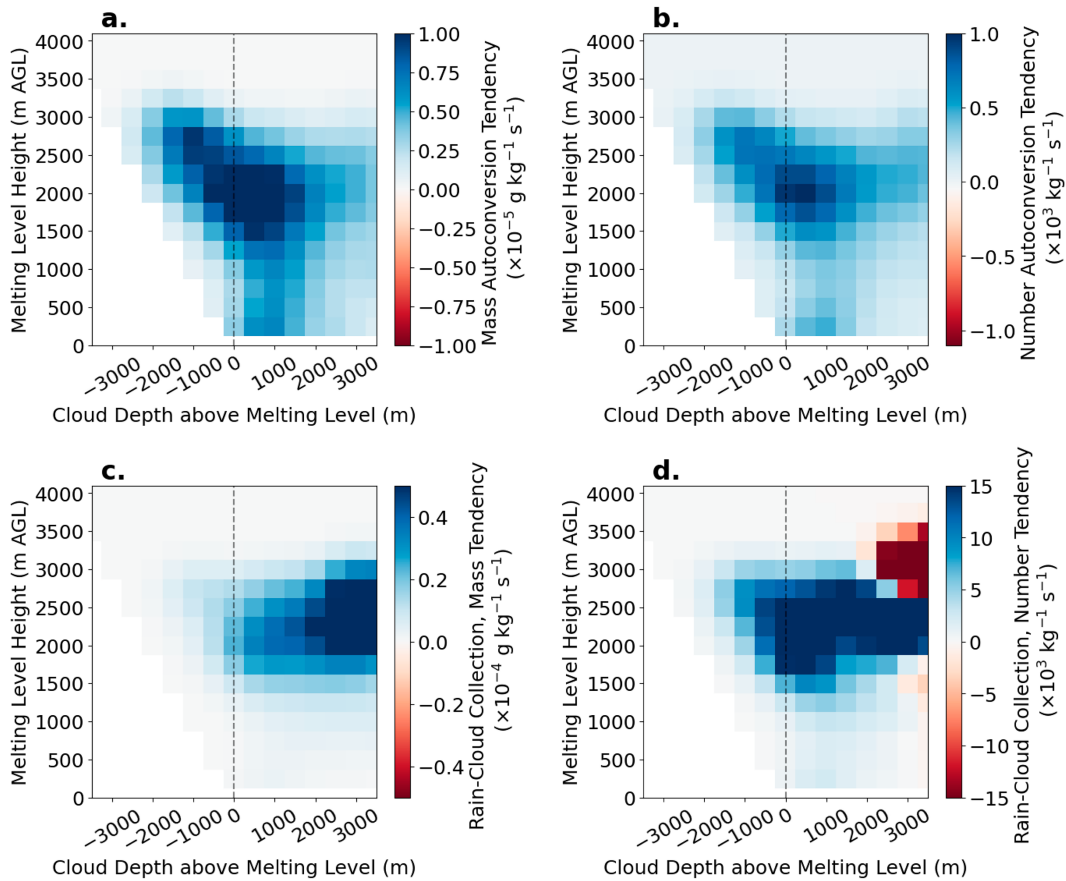


FIG. 10. As in Fig. 9, but displaying difference plots (RCON minus Control) of warm rain process rates: (a) autoconversion rain mass tendency, (b) autoconversion rain number tendency, (c) rain mass tendency from rain-cloud collection, and (d) cloud number tendency from rain-cloud collection. Note the values are adjusted by a constant to facilitate interpretation.

number concentration contributed to smaller raindrop diameters, a known property of warm rain, thus reducing the microphysical deficiencies documented by Conrick et al. (2019a,b) and Naeger et al. (2020). Finally, RCON performance was evaluated

relative to the mean of a 24-member real-time WRF ensemble system over the 1-yr period from August 2021 to August 2022. Results demonstrated more accurate precipitation forecasts from RCON across the Pacific Northwest, with the largest

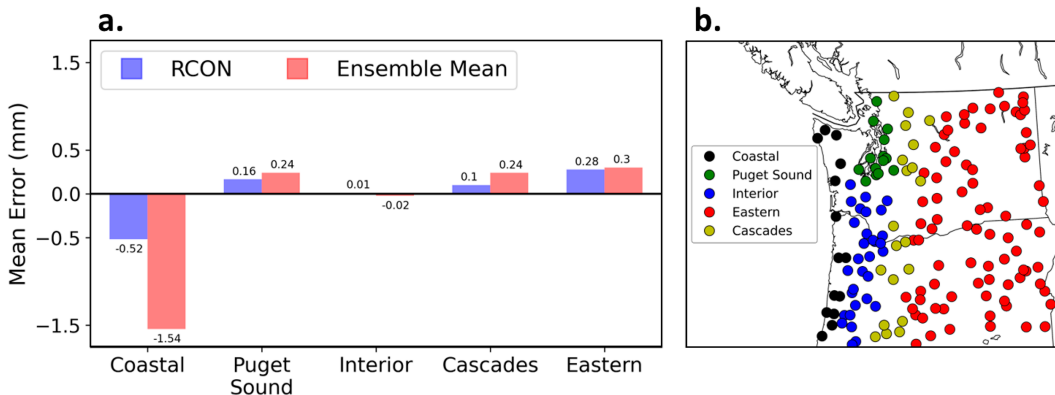


FIG. 11. (right) Map of observing stations (ASOS, AWOS, and RAWS) used to evaluate the real-time performance of RCON. Colored icons define different analysis regions. (left) Bar plots of mean error (forecast minus observed; mm) in each of the five analysis regions. The period considered is 15 Aug 2021–15 Aug 2022.

increase in accuracy over the Pacific coastal zone. Importantly, RCON did not degrade precipitation forecasts away from the Pacific coast.

As with any model development, it is important to note some sources of uncertainty and potential next steps. The formulation used for the lognormal distribution width parameter σ is a potential source of uncertainty. While our expression for σ as a function of N_C and Q_C was shown to realistically simulate precipitation, we plan to further investigate this parameter and refine its formulation. Second, numerical diffusion and/or vertical advection may be contributing to DSD broadening in the SBM scheme and therefore may be widening the lognormal DSDs we described in this study (i.e., Morrison et al. 2018, 2020b). Finally, although only two case studies were used to develop the microphysical modifications presented in this paper, the utility of RCON is supported by its successful application during the extended OLYMPEX period and during a 12-month period as a member of a real-time ensemble forecast system. While further work remains, the RCON microphysical modifications offer progress toward improving the prediction of warm rain over coastal areas and windward slopes of the Pacific Northwest and elsewhere.

Acknowledgments. The authors thank Drs. Joseph Boomgard-Zagrodnik, Daehyun Kim, Greg Thompson, Jacob Shpund, and Robert Wood for their collaboration, insightful discussions, and comments on this project; and to the anonymous reviewers for their comments that helped to greatly improve the manuscript. Thanks also to David Ovens for his support of this project, coming up with the name RCON, and implementation of the scheme into the UW WRF ensemble. We also thank the U.S. Forest Service, National Park Service, and the Quinault Indian Nation for their support of OLYMPEX. Financial support for the project was provided by Grants NSF AGS-2042105 and NSF AGS-1349847. We would like to acknowledge high-performance computing support from Cheyenne (doi: 10.5065/D6RX99HX) provided by NCAR's Computational and Information Systems Laboratory, sponsored by the National Science Foundation.

Data availability statement. All data used in this manuscript are freely available from the following sources or by request from the corresponding author, including WRF Model data, including namelists, are available upon request; GFS forecast grids, used for initial/boundary conditions, are available from the National Centers for Environmental Information (NCEI): <https://www.ncei.noaa.gov/products/weather-climate-models/global-forecast>; NARR grids can be obtained through the NCEI at <https://www.ncei.noaa.gov/products/weather-climate-models/north-american-regional>; MRR radar data from OLYMPEX can be obtained from NASA at: <http://doi.org/10.5067/GPMGV/OLYMPEX/MRR/DATA201>; PARSIVEL² data from OLYMPEX can be obtained from NASA at <http://doi.org/10.5067/GPMGV/OLYMPEX/APU/DATA301>; rawinsonde data can be obtained through the University of Wyoming upper-air website (<http://weather.uwyo.edu/upperair/sounding.html>) or upon request from the corresponding author; and the RCON model code is available from the corresponding author.

APPENDIX A

The Thompson–Eidhammer (TE14) and Hebrew University Of Jerusalem Bin (SBM) Schemes

a. The Thompson–Eidhammer scheme

The TE14 scheme predicts the mass mixing ratios of six microphysical species: cloud water, cloud ice, rainwater, snow, and graupel. Cloud water, rainwater, and cloud ice number concentrations are prognostic, thus making the scheme double-moment for those quantities. The scheme assumes exponential size distributions for all species except cloud water (gamma) and snow (sum of gamma and exponential). TE14 also simulates water- and ice-friendly aerosol number concentrations, which directly influence the cloud water and cloud ice number concentrations. The scheme is currently available in the Weather Research and Forecasting model (WRF; Skamarock et al. 2008). The predecessor to TE14, the Thompson et al. (2008) scheme, uses the same warm rain production processes and is employed by the National Centers for Environmental Prediction (NCEP) High-Resolution Rapid Refresh (HRRR) model.

b. The Hebrew University of Jerusalem bin model

The Hebrew University of Jerusalem (HUJI) Spectral Bin Model SBM scheme simulates evolving distributions of liquid and ice phase hydrometeors. Regarding liquid-phase DSDs, we use 33 mass-doubling liquid water bins that range in droplet radius from 2 μm to 32.5 μm , with the model simulating the collision–coalescence, break-up, condensation, and evaporation processes of liquid particles. Shpund et al. (2019) offers an extensive review of the SBM scheme.

Bin microphysics schemes are significantly more complex than bulk schemes because bin schemes do not assume the shape of hydrometeor size distributions, instead allowing the distributions to naturally evolve in response to microphysical processes (see the review articles of Khain et al. 2015 and Morrison et al. 2020a). Representing all liquid hydrometeors within a single, continuously evolving distribution produces more realistic, but more numerically expensive, microphysical simulations compared to the simplified integral representations of bulk microphysics schemes (Khain et al. 2015; Grabowski et al. 2019; Morrison et al. 2020a).

APPENDIX B

WRF-ARW Model Configurations

a. Configuration details

This appendix describes the model configurations of the several WRF-ARW Model simulations conducted in this study. All simulations used version 4.2.2 of the WRF-ARW Model applied to different domain configurations (described below). However, the distribution of vertical levels was the same for each simulation: 51 vertical levels spaced according to the model's hybrid vertical coordinate option (Klemp 2011), with the sigma-isobaric transition level set at its default of 0.2. Other model configuration options included the YSU PBL parameterization (Hong et al. 2006) and RRTMG radiation

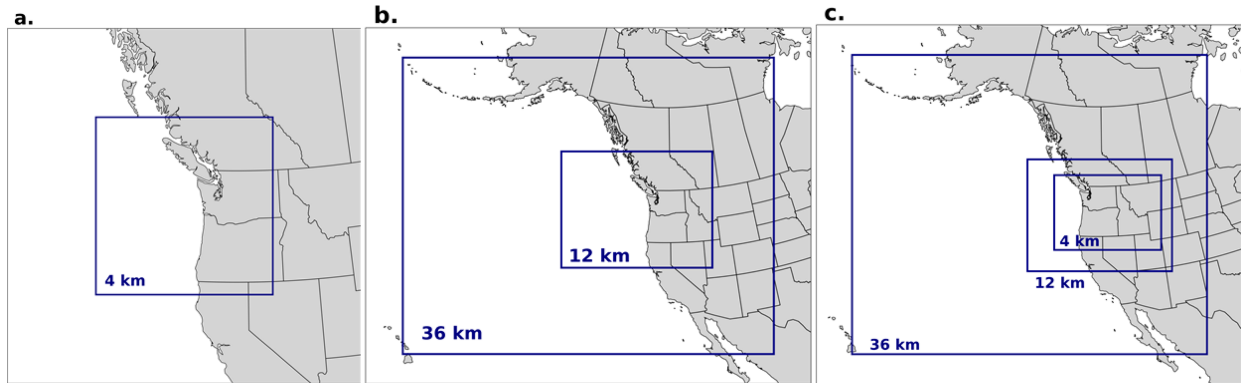


FIG. B1. WRF-ARW Model domains for (a) simulations of the 20 Sep 2015 and 15 Feb 2016 events, (b) extended-period (1 Nov–15 Dec 2015) simulations, and (c) real-time UW WRF ensemble.

scheme (Iacono et al. 2008). Initial and boundary conditions for all simulations were from the Global Forecast System 0.25° analysis. In addition to the above configuration:

- Simulations of the 20 September 2015 and 15 February 2016 events, which were used to develop RCON, applied a single domain with 4-km horizontal grid spacing that was centered offshore of the Pacific Northwest (Fig. B1a). Simulations of these events were conducted using TE14, RCON, and the HUJI SBM microphysics. No cumulus parameterization was used. For the 20 September 2015 event, simulations were run for 36 h from 1200 UTC 19 September to 0000 UTC 21 September 2015; simulations of the 15 February 2016 event were run for 24 h starting at 0000 UTC 15 February 2016.
- The extended simulation (1 November 2015–15 December 2016) used a nested 36- to 12-km grid spacing for its horizontal configuration (Fig. B1b). This simulation was run using TE14 and RCON microphysics. The Grell-Freitas cumulus scheme (Grell and Freitas 2014) was applied to both domains. The simulation was initialized at 0000 UTC 1 November 2015 and integrated for 45 days.
- The University of Washington WRF ensemble forecast system has a nested domain configuration, with a 4-km horizontal grid spacing on the innermost domain which covers all of the Pacific Northwest (Fig. B1c).

Only the innermost domains were used for the analyses presented in this manuscript.

b. Simulated aerosol information

While a comprehensive evaluation of aerosols is outside of the scope of this project, it is important to note how each scheme simulates aerosols as part of the model’s configuration. Aerosols in the Control (TE14) simulation follow that scheme’s climatological aerosol method, whereby several aerosol species derived from monthly averages of multiyear GOCART aerosol data were processed and averaged together into a single aerosol type represented by a single lognormal aerosol distribution. In TE14, those aerosols are then nucleated into cloud droplets according to the results of a parcel model that are acquired through

a lookup table. Users of TE14 can select aerosol radius and hygroscopicity; in this work we apply the default values (0.04 μm and 0.4, respectively). For more information, see Thompson and Eidhammer (2014). The SBM scheme uses a more complex trimodal aerosol distribution with user-selected chemical properties. The properties of each mode (size, width, number concentration) can also be selected by the user. The SBM scheme then explicitly nucleates aerosols based on the aerosol’s properties and the nucleated mass is placed into the smallest cloud droplet bin. Spatially, there are different aerosol distributions for maritime and continental land surfaces. We retain the default aerosol configuration from the SBM scheme, though as mentioned in section 2, simulations are not sensitive to aerosol configuration. Additional information for the SBM scheme can be found in Shpund et al. (2019). For both schemes, aerosols are allowed to advect throughout the domain.

APPENDIX C

Determination of the Lognormal Width Parameter

The width parameter of the lognormal distribution, σ , is a key quantity for the cloud DSD. Like its counterpart for a gamma distribution μ , the parameter σ must be estimated by observations or model data. This approach has been used in previous studies to diagnose the gamma shape parameter μ (Brandes et al. 2004; Bringi et al. 2002; Cao et al. 2008; Zhang et al. 2003, 2006).

Our goal was to create an expression for σ that is dependent only on N_C and Q_C , which are available within the bulk scheme. The process of producing a functional form of σ was as follows: From the SBM scheme, cloud DSDs were obtained from the 20 September 2015 and 15 February 2016 events from offshore, coastal, and windward regions of the Olympic Peninsula. These distributions were then integrated to calculate the effective diameters (D_e) according to Eq. (C1). Next, the median diameter \bar{D}_N can be calculated if D_e and σ are known, as shown in Eq. (C2):

$$D_e = \frac{\int D^3 N(D) dD}{\int D^2 N(D) dD} = \bar{D}_N \exp\left(\frac{5}{2}\sigma^2\right), \quad (C1)$$

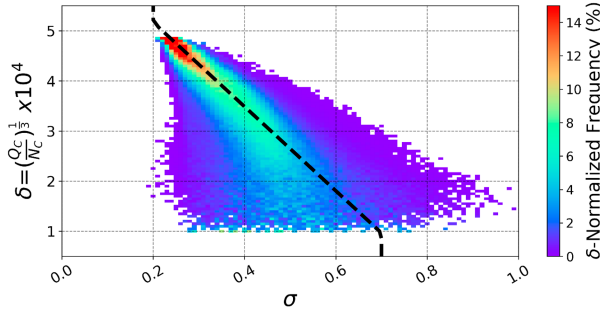


FIG. C1. Frequency distribution of σ as a function of $\delta = 10^4 \times (Q_C/N_C)^{1/3}$, with data obtained from the SBM scheme over the dashed region of Fig. S1 during the 20 Sep 2015 and 15 Feb 2016 events. A description of δ is provided in appendix C. Data are normalized by δ to produce the linear fit shown. The black line represents the functional form of σ used in RCON.

$$\widetilde{D}_N = D_e \exp\left(-\frac{5}{2}\sigma^2\right). \quad (\text{C2})$$

Next, the equation for cloud water mass mixing ratio, Q_C , Eq. (C3), is solved for σ after substituting \widetilde{D}_N with Eq. (C2):

$$Q_C = \frac{\pi\rho_w N_T \widetilde{D}_N^3}{6} \exp\left(\frac{9\sigma^2}{2}\right). \quad (\text{C3})$$

The result of this process is shown in Eq. (C4), where LOG is the natural logarithm:

$$\sigma = \left[-\frac{1}{3} \text{LOG}\left(\frac{6Q_C}{\pi\rho_w N_C D_e^3}\right) \right]^{1/2}. \quad (\text{C4})$$

By analyzing the relationships between Q_C , N_C , and σ from the SBM, it was determined that using a simplified diameter expression, defined as $\delta = (Q_C/N_C)^{1/3}$, was easily calculable and produced the strongest relationship between the quantities (Fig. C1). The functional form of σ used in RCON is a linear relationship between δ and σ , as shown in Fig. C1 and Eq. (C5), which is limited to the range of $\sigma = [0.2, 0.7]$. Future work by the authors will continue to refine the expression for σ :

$$\sigma = \begin{cases} 0.2, & \text{if } \delta > 5.5 \times 10^{-4}, \\ (-1.19 \times 10^3)\delta + 0.815, & \text{if } 0.9 \times 10^{-4} < \delta < 5.5 \times 10^{-4}, \\ 0.7, & \text{if } \delta > 0.9 \times 10^{-4}. \end{cases} \quad (\text{C5})$$

APPENDIX D

Autoconversion

This section compares the autoconversion formula we use (from Nickerson et al. 1986) to autoconversion in the Thompson–Eidhammer (TE14, Thompson and Eidhammer 2014) microphysics scheme. Both mass autoconversion equations are derived from the parameterization of Berry

and Reinhardt (1974, hereafter BR74), which has been used in microphysical parameterizations since its debut. Interested readers are directed to the review by Gilmore and Straka (2008), which describes in detail the mechanics of the BR74 scheme, its many variations, and a number of its uses throughout the literature.

Relevant to RCON is the lognormal adaptation of BR74 from Nickerson et al. (1986), which adjusts the appropriate characteristic droplet diameters and other parameters to account for the lognormal cloud water distribution. We incorporate the Nickerson et al. (1986) autoconversion equations into the WRF Model as follows. The rate of change of rainwater mass due to autoconversion of cloud water is

$$\frac{dQ_R}{dt} = 0.067\rho_{\text{air}}Q_C^2 \left[10^{16} \left(\frac{\rho_{\text{air}}Q_C}{N_C} \right)^{4/3} \sqrt{\text{varx}} - 2.7 \right] \times \left[10^4 \left(\frac{\rho_{\text{air}}Q_C \sqrt{\text{varx}}}{N_C} \right)^{1/3} - 1.2 \right] \quad (\text{kg kg}^{-1} \text{ s}^{-1}), \quad (\text{D1})$$

where $\text{varx} = \exp(9\sigma^2) - 1$ is a variance parameter for the cloud DSD, Q_R is the rainwater mixing ratio (kg kg^{-1}), Q_C is the cloud water mixing ratio (kg kg^{-1}), N_C is the cloud number droplet concentration (kg^{-1}), ρ_{air} is the density of air (kg m^{-3}), and σ is the width of the lognormal cloud water distribution.

The TE14 microphysics scheme used in Control simulations throughout this study also uses the BR74 autoconversion parameterization, but with a different formulation:

$$\frac{dQ_R}{dt} = \frac{0.027\rho_{\text{air}}Q_C \left(\frac{1}{16} \times 10^{20} D_b^3 D_f - 0.4 \right)}{Q_C \rho_{\text{air}} \left(\frac{1}{2} \times 10^6 D_b - 7.5 \right)^{-1}} \quad (\text{kg kg}^{-1} \text{ s}^{-1}), \quad (\text{D2})$$

where

$$D_f = \left(\frac{6\rho_{\text{air}}Q_C}{\pi\rho_w N_C} \right)^{1/3}, \quad D_g = \frac{\left[\frac{\Gamma(\mu_C + 7)}{\Gamma(\mu_C + 4)} \right]^{1/3}}{\lambda_C}, \quad \text{and}$$

$$D_b = (D_f^3 D_g^3 - D_f^6)^{1/6}$$

are various characteristic diameters of the gamma cloud water distribution, ρ_w is the density of liquid water (kg m^{-3}), and μ_C is the shape parameter of the gamma cloud water distribution. Q_C and N_C have the same units as in Eq. (D1).

The use of Nickerson et al. (1986) autoconversion increases the amount of cloud water that is converted to rain (see Fig. 5 in the manuscript and supplement 2). Comparing the functional form of autoconversion from RCON and TE14 shows that the average autoconversion rate increases from $2.06 \times 10^{-5} \text{ g m}^{-3} \text{ s}^{-1}$ in the TE14 autoconversion parameterization to $1.35 \times 10^{-4} \text{ g m}^{-3} \text{ s}^{-1}$.

Next, the change in rain number concentration due to autoconversion is considered. The general bulk formulation for this process is

$$\frac{dN_R}{dt} = \frac{\frac{dQ_R}{dt}}{\alpha \frac{\pi}{6} D_0^3} \quad (\text{kg}^{-1} \text{s}^{-1}), \quad (\text{D3})$$

where dQ_R/dt is the mass autoconversion rate ($\text{kg kg}^{-1} \text{s}^{-1}$), N_R is the raindrop number concentration (kg^{-3}), D_0 is the minimum raindrop diameter (mm), and α is a constant.

In TE14, $D_0 = 50 \mu\text{m}$ and $\alpha = 200\mu_c$ where μ_c is the gamma distribution shape parameter, an integer calculated as a function of cloud droplet number concentration according to $\mu_c = \max(15, 1 \times 10^9/N_C + 2)$, which bounds the shape parameter between 2 and 15 with larger N_C corresponding to smaller μ_c . N_C in the expression of μ_c has units of m^{-3} . In the TE14 scheme, when $N_C \cong 10^8 \text{m}^{-3}$ (a typical value of N_C), the number of raindrops produced by autoconversion is reduced by a factor of ~ 600 , compared to a denominator without α , which is partially responsible for the large rain diameters described in the manuscript.

In contrast, the Nickerson et al. (1986) autoconversion scheme uses a smaller D_0 ($32 \mu\text{m}$) and $\alpha = 1$ in its default configuration. The selection of these values results in significantly too many raindrops of very small size being produced, causing poor agreement with observations. Consequently, the RCON retains $D_0 = 50 \mu\text{m}$ from TE14 and sets $\alpha = 200$. By neglecting the distribution width in formulating α , more raindrops are produced. This combination of parameters was found to produce the best balance of rain number concentration and raindrop diameter. Future work by the authors will investigate whether α should exhibit a functional form.

REFERENCES

- Abel, S. J., and I. A. Boutle, 2012: An improved representation of the raindrop size distribution for single moment microphysics schemes. *Quart. J. Roy. Meteor. Soc.*, **138**, 2151–2162, <https://doi.org/10.1002/qj.1949>.
- Ahmed, T., H.-G. Jin, and J.-J. Baik, 2020: A physically based raindrop–cloud droplet accretion parametrization for use in bulk microphysics schemes. *Quart. J. Roy. Meteor. Soc.*, **146**, 3368–3383, <https://doi.org/10.1002/qj.3850>.
- Barros, A. P., P. Shrestha, S. Chavez, and Y. Duan, 2018: Modeling aerosol–cloud–precipitation interactions in mountainous regions: Challenges in the representation of indirect microphysical effects with impacts at subregional scales. *Rainfall—Extremes, Distribution, and Properties*, J. Abbot and A. Hammond, Eds., IntechOpen, <https://doi.org/10.5772/intechopen.80025>.
- Berry, E. X., and R. L. Reinhardt, 1974: An analysis of cloud drop growth by collection. Part IV: A new parameterization. *J. Atmos. Sci.*, **31**, 2127–2135, [https://doi.org/10.1175/1520-0469\(1974\)031<2127:AAOCDG>2.0.CO;2](https://doi.org/10.1175/1520-0469(1974)031<2127:AAOCDG>2.0.CO;2).
- Brandes, E. A., G. Zhang, and J. Vivekanandan, 2004: Comparison of polarimetric radar drop size distribution retrieval algorithms. *J. Atmos. Oceanic Technol.*, **21**, 584–598, [https://doi.org/10.1175/1520-0426\(2004\)021<0584:COPRDS>2.0.CO;2](https://doi.org/10.1175/1520-0426(2004)021<0584:COPRDS>2.0.CO;2).
- Bringi, V. N., G.-J. Huang, V. Chandrasekar, and E. Gorgucci, 2002: A methodology for estimating the parameters of a gamma raindrop size distribution model from polarimetric radar data: Application to a squall-line event from the TRMM/Brazil campaign. *J. Atmos. Oceanic Technol.*, **19**, 633–645, [https://doi.org/10.1175/1520-0426\(2002\)019<0633:AMFETP>2.0.CO;2](https://doi.org/10.1175/1520-0426(2002)019<0633:AMFETP>2.0.CO;2).
- Cao, Q., G. Zhang, E. Brandes, T. Schuur, A. Ryzhkov, and K. Ikeda, 2008: Analysis of video disdrometer and polarimetric radar data to characterize rain microphysics in Oklahoma. *J. Appl. Meteor. Climatol.*, **47**, 2238–2255, <https://doi.org/10.1175/2008JAMC1732.1>.
- Colle, B. A., and C. F. Mass, 2000: The 5–9 February 1996 flooding event over the Pacific Northwest: Sensitivity studies and evaluation of the MM5 precipitation forecasts. *Mon. Wea. Rev.*, **128**, 593–617, [https://doi.org/10.1175/1520-0493\(2000\)128<0593:TFFEOT>2.0.CO;2](https://doi.org/10.1175/1520-0493(2000)128<0593:TFFEOT>2.0.CO;2).
- , K. J. Westrick, and C. F. Mass, 1999: Evaluation of MM5 and Eta-10 precipitation forecasts over the Pacific Northwest during the cool season. *Wea. Forecasting*, **14**, 137–154, [https://doi.org/10.1175/1520-0434\(1999\)014<0137:EOMAEP>2.0.CO;2](https://doi.org/10.1175/1520-0434(1999)014<0137:EOMAEP>2.0.CO;2).
- Conrick, R., and C. F. Mass, 2019a: Evaluating simulated microphysics during OLYMPEX using GPM satellite observations. *J. Atmos. Sci.*, **76**, 1093–1105, <https://doi.org/10.1175/JAS-D-18-0271.1>.
- , and —, 2019b: An evaluation of simulated precipitation characteristics during OLYMPEX. *J. Hydrometeorol.*, **20**, 1147–1164, <https://doi.org/10.1175/JHM-D-18-0144.1>.
- Darby, L. S., A. B. White, D. J. Gottas, and T. Coleman, 2019: An evaluation of integrated water vapor, wind, and precipitation forecasts using water vapor flux observations in the western United States. *Wea. Forecasting*, **34**, 1867–1888, <https://doi.org/10.1175/WAF-D-18-0159.1>.
- Duan, Y., M. D. Petters, and A. P. Barros, 2019: Understanding aerosol–cloud interactions through modeling the development of orographic cumulus congestus during IPHEX. *Atmos. Chem. Phys.*, **19**, 1413–1437, <https://doi.org/10.5194/acp-19-1413-2019>.
- Garreaud, R., M. Falvey, and A. Montecinos, 2016: Orographic precipitation in coastal southern Chile: Mean distribution, temporal variability, and linear contribution. *J. Hydrometeorol.*, **17**, 1185–1202, <https://doi.org/10.1175/JHM-D-15-0170.1>.
- Garvert, M. F., C. P. Woods, B. A. Colle, C. F. Mass, P. V. Hobbs, M. T. Stoelinga, and J. B. Wolfe, 2005a: The 13–14 December 2001 IMPROVE-2 event. Part II: Comparisons of MM5 model simulations of clouds and precipitation with observations. *J. Atmos. Sci.*, **62**, 3520–3534, <https://doi.org/10.1175/JAS3551.1>.
- Geoffroy, O., A. P. Siebesma, and F. Burnet, 2014: Characteristics of the raindrop distributions in RICO shallow cumulus. *Atmos. Chem. Phys.*, **14**, 10897–10909, <https://doi.org/10.5194/acp-14-10897-2014>.
- Gilmore, M. S., and J. M. Straka, 2008: The Berry and Reinhardt autoconversion parameterization: A digest. *J. Appl. Meteor. Climatol.*, **47**, 375–396, <https://doi.org/10.1175/2007JAMC1573.1>.
- Grabowski, W. W., H. Morrison, S.-I. Shima, G. C. Abade, P. Dziekan, and H. Pawlowska, 2019: Modeling of cloud microphysics: Can we do better? *Bull. Amer. Meteor. Soc.*, **100**, 655–672, <https://doi.org/10.1175/BAMS-D-18-0005.1>.
- Grell, G. A., and S. R. Freitas, 2014: A scale and aerosol aware stochastic convective parameterization for weather and air quality modeling. *Atmos. Chem. Phys.*, **14**, 5233–5250, <https://doi.org/10.5194/acp-14-5233-2014>.
- Hong, S.-Y., Y. Noh, and J. Dudhia, 2006: A new vertical diffusion package with an explicit treatment of entrainment processes. *Mon. Wea. Rev.*, **134**, 2318–2341, <https://doi.org/10.1175/MWR3199.1>.

- Houze, R. A., Jr., and Coauthors, 2017: The Olympic Mountains experiment (OLYMPEX). *Bull. Amer. Meteor. Soc.*, **98**, 2167–2188, <https://doi.org/10.1175/BAMS-D-16-0182.1>.
- Iacono, M. J., J. S. Delamere, E. J. Mlawer, M. W. Shephard, S. A. Clough, and W. D. Collins, 2008: Radiative forcing by long-lived greenhouse gases: Calculations with the AER radiative transfer models. *J. Geophys. Res.*, **113**, D13103, <https://doi.org/10.1029/2008JD009944>.
- Khain, A. P., and Coauthors, 2015: Representation of microphysical processes in cloud-resolving models: Spectral (bin) microphysics versus bulk parameterization. *Rev. Geophys.*, **53**, 247–322, <https://doi.org/10.1002/2014RG000468>.
- Khairoutdinov, M., and Y. Kogan, 2000: A new cloud physics parameterization in a large-eddy simulation model of marine stratocumulus. *Mon. Wea. Rev.*, **128**, 229–243, [https://doi.org/10.1175/1520-0493\(2000\)128<0229:ANCPPI>2.0.CO;2](https://doi.org/10.1175/1520-0493(2000)128<0229:ANCPPI>2.0.CO;2).
- Klemp, J. B., 2011: A terrain-following coordinate with smoothed coordinate surfaces. *Mon. Wea. Rev.*, **139**, 2163–2169, <https://doi.org/10.1175/MWR-D-10-05046.1>.
- Lee, H., and J.-J. Baik, 2017: A physically based autoconversion parameterization. *J. Atmos. Sci.*, **74**, 1599–1616, <https://doi.org/10.1175/JAS-D-16-0207.1>.
- Lim, K.-S. S., and S.-Y. Hong, 2010: Development of an effective double-moment cloud microphysics scheme with prognostic cloud condensation nuclei (CCN) for weather and climate models. *Mon. Wea. Rev.*, **138**, 1587–1612, <https://doi.org/10.1175/2009MWR2968.1>.
- Lin, Y., and B. A. Colle, 2009: The 4–5 December 2001 IMPROVE-2 event: Observed microphysics and comparisons with the Weather Research and Forecasting Model. *Mon. Wea. Rev.*, **137**, 1372–1392, <https://doi.org/10.1175/2008MWR2653.1>.
- , —, and S. E. Yuter, 2013: Impact of moisture flux and freezing level on simulated orographic precipitation errors over the Pacific Northwest. *J. Hydrometeorol.*, **14**, 140–152, <https://doi.org/10.1175/JHM-D-12-019.1>.
- Mansell, E. R., C. L. Ziegler, and E. C. Bruning, 2010: Simulated electrification of a small thunderstorm with two-moment bulk microphysics. *J. Atmos. Sci.*, **67**, 171–194, <https://doi.org/10.1175/2009JAS2965.1>.
- Massmann, A. K., J. R. Minder, R. D. Garreaud, D. E. Kingsmill, R. A. Valenzuela, A. Montecinos, S. L. Fults, and J. R. Snider, 2017: The Chilean coastal orographic precipitation experiment: Observing the Influence of microphysical rain regimes on coastal orographic precipitation. *J. Hydrometeorol.*, **18**, 2723–2743, <https://doi.org/10.1175/JHM-D-17-0005.1>.
- McMurdie, L. A., A. K. Rowe, R. A. Houze Jr., S. R. Brodzik, J. P. Zagrodnik, and T. M. Schuldt, 2018: Terrain-enhanced precipitation processes above the melting layer: Results from OLYMPEX. *J. Geophys. Res. Atmos.*, **123**, 12194–12209, <https://doi.org/10.1029/2018JD029161>.
- Miles, N. L., J. Verlinde, and E. E. Clothiaux, 2000: Cloud droplet size distributions in low-level stratiform clouds. *J. Atmos. Sci.*, **57**, 295–311, [https://doi.org/10.1175/1520-0469\(2000\)057<0295:CDSDIL>2.0.CO;2](https://doi.org/10.1175/1520-0469(2000)057<0295:CDSDIL>2.0.CO;2).
- Min, K.-H., S. Choo, D. Lee, and G. Lee, 2015: Evaluation of WRF cloud microphysics schemes using radar observations. *Wea. Forecasting*, **30**, 1571–1589, <https://doi.org/10.1175/WAF-D-14-00095.1>.
- Minder, J. R., D. R. Durran, G. H. Roe, and A. M. Anders, 2008: The climatology of small-scale orographic precipitation over the Olympic Mountains: Patterns and processes. *Quart. J. Roy. Meteor. Soc.*, **134**, 817–839, <https://doi.org/10.1002/qj.258>.
- Morrison, H., M. Witte, G. H. Bryan, J. Y. Harrington, and Z. J. Lebo, 2018: Broadening of modeled cloud droplet spectra using bin microphysics in an Eulerian spatial domain. *J. Atmos. Sci.*, **75**, 4005–4030, <https://doi.org/10.1175/JAS-D-18-0055.1>.
- , and Coauthors, 2020a: Confronting the challenge of modeling cloud and precipitation microphysics. *J. Adv. Model. Earth Syst.*, **12**, e2019MS001689, <https://doi.org/10.1029/2019MS001689>.
- , M. van Lier-Walqui, M. R. Kumjian, and O. P. Prat, 2020b: A Bayesian approach for statistical-physical bulk parameterization of rain microphysics. Part I: Scheme description. *J. Atmos. Sci.*, **77**, 1019–1041, <https://doi.org/10.1175/JAS-D-19-0070.1>.
- Naeger, A. R., B. A. Colle, N. Zhou, and A. Molthan, 2020: Evaluating warm and cold rain processes in cloud microphysical schemes using OLYMPEX field measurements. *Mon. Wea. Rev.*, **148**, 2163–2190, <https://doi.org/10.1175/MWR-D-19-0092.1>.
- Nickerson, E. C., E. Richard, R. Rosset, and D. R. Smith, 1986: The numerical simulation of clouds, rains and airflow over the Vosges and Black Forest mountains: A meso- β model with parameterized microphysics. *Mon. Wea. Rev.*, **114**, 398–414, [https://doi.org/10.1175/1520-0493\(1986\)114<0398:TNSOCR>2.0.CO;2](https://doi.org/10.1175/1520-0493(1986)114<0398:TNSOCR>2.0.CO;2).
- Schumacher, V., A. Fernández, F. Justino, and A. Comin, 2020: WRF high resolution dynamical downscaling of precipitation for the Central Andes of Chile and Argentina. *Front. Earth Sci.*, **8**, 328, <https://doi.org/10.3389/feart.2020.00328>.
- Seifert, A., and K. D. Beheng, 2001: A double-moment parameterization for simulating autoconversion, accretion and self-collection. *Atmos. Res.*, **59–60**, 265–281, [https://doi.org/10.1016/S0169-8095\(01\)00126-0](https://doi.org/10.1016/S0169-8095(01)00126-0).
- , and —, 2006: A two-moment cloud microphysics parameterization for mixed-phase clouds. Part 1: Model description. *Meteor. Atmos. Phys.*, **92**, 45–66, <https://doi.org/10.1007/s00703-005-0112-4>.
- Sena, E. T., A. McComiskey, and G. Feingold, 2016: A long-term study of aerosol–cloud interactions and their radiative effect at the southern Great Plains using ground-based measurements. *Atmos. Chem. Phys.*, **16**, 11 301–11 318, <https://doi.org/10.5194/acp-16-11301-2016>.
- Shpund, J., and Coauthors, 2019: Simulating a mesoscale convective system using WRF with a new spectral bin microphysics. 1: Hail vs graupel. *J. Geophys. Res. Atmos.*, **124**, 14 072–14 101, <https://doi.org/10.1029/2019JD030576>.
- Skamarock, W. C., and Coauthors, 2008: A description of the Advanced Research WRF version 3. NCAR Tech. Note NCAR/TN-475+STR, 113 pp., <https://doi.org/10.5065/D68S4MVH>.
- Song, H.-J., and B.-J. Sohn, 2018: An evaluation of WRF microphysics schemes for simulating the warm-type heavy rain over the Korean Peninsula. *Asia-Pac. J. Atmos. Sci.*, **54**, 225–236, <https://doi.org/10.1007/s13143-018-0006-2>.
- Thompson, G., and T. Eidhammer, 2014: A study of aerosol impacts on clouds and precipitation development in a large winter cyclone. *J. Atmos. Sci.*, **71**, 3636–3658, <https://doi.org/10.1175/JAS-D-13-0305.1>.
- , P. R. Field, R. M. Rasmussen, and W. D. Hall, 2008: Explicit forecasts of winter precipitation using an improved bulk microphysics scheme. Part II: Implementation of a new snow parameterization. *Mon. Wea. Rev.*, **136**, 5095–5115, <https://doi.org/10.1175/2008MWR2387.1>.
- Thurai, M., P. Gatlin, V. N. Bringi, W. Petersen, P. Kennedy, B. Notaroš, and L. Carey, 2017: Toward completing the raindrop size spectrum: Case studies involving 2D-video disdrometer, droplet spectrometer, and polarimetric radar measurements. *J. Appl. Meteor. Climatol.*, **56**, 877–896, <https://doi.org/10.1175/JAMC-D-16-0304.1>.

- , V. Bringi, P. N. Gatlin, W. A. Petersen, and M. T. Wingo, 2019: Measurements and modeling of the full rain drop size distribution. *Atmosphere*, **10**, 39, <https://doi.org/10.3390/atmos10010039>.
- Wang, L.-P., O. Ayala, B. Rosa, and W. W. Grabowski, 2008: Turbulent collision efficiency of heavy particles relevant to cloud droplets. *New J. Phys.*, **10**, 075013, <https://doi.org/10.1088/1367-2630/10/7/075013>.
- Zagrodnik, J. P., L. A. McMurdie, and R. A. Houze, Jr., 2018: Stratiform precipitation processes in cyclones passing over a coastal mountain range. *J. Atmos. Sci.*, **75**, 983–1004, <https://doi.org/10.1175/JAS-D-17-0168.1>.
- , —, —, and S. Tanelli, 2019: Vertical structure and microphysical characteristics of frontal systems passing over a three-dimensional coastal mountain range. *J. Atmos. Sci.*, **76**, 1521–1546, <https://doi.org/10.1175/JAS-D-18-0279.1>.
- Zeng, X., and X. Li, 2020: A two-moment bulk parameterization of the drop collection growth in warm clouds. *J. Atmos. Sci.*, **77**, 797–811, <https://doi.org/10.1175/JAS-D-19-0015.1>.
- Zhang, G., J. Vivekanandan, E. A. Brandes, R. Meneghini, and T. Kozi, 2003: The shape–slope relation in observed gamma raindrop size distributions: Statistical error or useful information? *J. Atmos. Oceanic Technol.*, **20**, 1106–1119, [https://doi.org/10.1175/1520-0426\(2003\)020<1106:TSRIOG>2.0.CO;2](https://doi.org/10.1175/1520-0426(2003)020<1106:TSRIOG>2.0.CO;2).
- , J. Sun, and E. A. Brandes, 2006: Improving parameterization of rain microphysics with disdrometer and radar observations. *J. Atmos. Sci.*, **63**, 1273–1290, <https://doi.org/10.1175/JAS3680.1>.